Electron capture and target excitation in intermediate-energy He+-H collisions

J. W. Gao [1,*] Y. Y. Qi,[2] Y. Wu,[3,4] J. G. Wang,[3] N. Sisourat,[5] and A. Dubois[5]

[1]*School of Physics, Hangzhou Normal University, 311121 Hangzhou, China*
[2]*College of Data Science, Jiaxing University, Jiaxing 314001, China*
[3]*Key Laboratory of Computational Physics, Institute of Applied Physics and Computational Mathematics, 100088 Beijing, China*
[4]*Center for Applied Physics and Technology, HEDPS, Peking University, 100871 Beijing, China*
[5]*Sorbonne Université, CNRS, UMR 7614, Laboratoire de Chimie Physique-Matière et Rayonnement, 75005 Paris, France*

We present all-electron close-coupling calculations of cross sections for electron capture and target excitation occurring in 0.25–200 keV/u He+-H collisions. We show overall good agreements with available experimental data for total electron capture, $n = 2$ target excitation, and related H_α emission. We especially focus on $n\ell$-selective capture and excitation processes and critically compare our results with those from previous theoretical investigations. Our results confirm the oscillatory structures observed in the spin-averaged H(2s) and H(2p) excitation cross sections for impact energies below 50 keV/u. Furthermore, we interpret these oscillations as the consequence of interferences between excitation to H(2s) and H(2p_0) in both spin-singlet and spin-triplet symmetries, as well as between electron capture to He($1s2p$ ^1P, $|M_L| = 1$) and excitation to H($2p_1$) in spin-singlet symmetry.

I. INTRODUCTION

Electron capture and target excitation in He+-H collisions have been the subject of both experimental and theoretical studies for a considerable time [1–25]. Indeed, these low-Z elements are the dominant constituents of astrophysical [26,27] and fusion [28,29] plasmas. In magnetic confinement fusion sciences, the neutral beam injection is a standard method to either heat or diagnose the plasmas [30,31]. Modeling of beam penetration into the plasma and of photoemission signals relies on detailed data for electronic processes occurring in ion-atom collisions [32]. On the other hand, from a fundamental point of view, such collision systems are also of challenging importance in relation to dynamical correlations between the target electron and the projectile one in the collision process. These two aspects make the study of the He+-H collision system interesting and quite challenging.

For total electron capture,

$$He^+(1s) + H(1s) \rightarrow He + H^+, \qquad (1)$$

cross sections were previously measured by Olson *et al.* [3] in the energy range of 2–100 keV/u, by Shah and Gilbody [33] from 15 to 115 keV/u, and by Hvelplund and Andersen [6] from 100 to 625 keV/u. Note that these experiments were performed with both dihydrogen and atomic hydrogen, produced by thermal dissociation of H_2 in a heated tungsten tube [34]. These results were found to be in reasonable agreement with later theoretical investigations based on various approaches to describe the collision dynamics in a specific energy domain: (i) the full quantum-mechanical molecular orbital close-coupling (QMOCC) method at low energies [24],

(ii) the semiclassical atomic orbital close-coupling (AOCC) method at intermediate energies [13,17,24], and (iii) the four-body continuum-distorted-wave (CDW-4B) perturbative treatment for high-impact energies [19]. However, for the state-selective electron capture processes, no experimental investigation has been reported so far and the only theoretical results by Liu *et al.* [24] are available. These authors use both QMOCC and AOCC approaches but the respective cross sections did not agree with each other in the overlapping energy region (around 1 keV/u) where these two methods may be expected to be valid, as long as convergence in the close-coupling scheme is reached.

For state-selective target excitation processes,

$$He^+(1s) + H(1s) \rightarrow He^+(1s) + H^*(n\ell), \qquad (2)$$
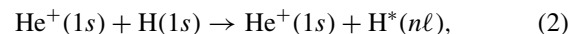
investigations are more scare. For atomic and molecular hydrogen targets, measurements were performed for H(2ℓ) excitation using the modulated crossed-beam technique in the energy ranges 1.25–6.5 and 2.5–25 keV/u, respectively [4,15]. These two series of experiments show oscillating cross sections as a function of impact energy. A complete explanation of this behavior is still missing.

For H(3ℓ) excitation, Donnelly *et al.* [11] have measured the cross sections for Balmer H_α emission in the energy range of 2.5–25 keV/u. These outcomes compare reasonably with AOCC calculations [13,17,24] for energies below 10 keV/u, while for higher energies large discrepancies exist between these four series of cross sections. For excitation to higher states, to the best of our knowledge, theoretical and experimental results are needed.

In this work, the processes of total and selective electron capture, respectively, Eq. (1) and

$$He^+(1s) + H(1s) \rightarrow He(1sn\ell \, ^{1,3}L) + H^+, \qquad (3)$$
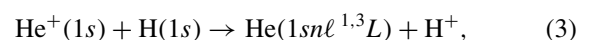
*gaojunwen@hznu.edu.cn

for $n = 2$ and 3, as well as target excitation, Eq. (2) ($n = 2 - 4$), are investigated in a wide energy domain ranging from 0.25 to 200 keV/u. We use a fully correlated (configuration interaction type) two-active-electron semiclassical asymptotic-state close-coupling (SCASCC) method. We are aiming to (i) provide accurate collisional cross sections, (ii) resolve the discrepancies with the existing data, and (iii) understand the oscillatory structures observed in the $n\ell$-selective target excitation cross sections.

The paper is set out as follows. In Sec. II we briefly outline the SCASCC method used in the present calculations. Section III is devoted to the detailed analysis of the electron capture and target excitation cross sections, including direct comparisons with available experimental and theoretical results. Conclusions are given in Sec. IV. Atomic units are used throughout, unless explicitly indicated.

II. THEORY

In the present work, the cross sections of the electronic processes occurring during He$^+$-H collisions are calculated within a semiclassical asymptotic-state close-coupling approach which has been previously described, for example, in Refs. [35–38]. We only outline briefly the main features of the method, with some details related to the present collision system considered. The two-electron time-dependent Schrödinger equation is written as

$$\left[H_e - i\frac{\partial}{\partial t} \right] \Psi(\vec{r}_1, \vec{r}_2, t) = 0, \tag{4}$$

where H_e is the electronic Hamiltonian

$$H_e = \sum_{i=1,2} \left[-\frac{1}{2}\nabla_i^2 + V_T(r_i) + V_P(r_i^p) \right] + \frac{1}{|\vec{r}_1 - \vec{r}_2|}, \tag{5}$$

and $\vec{r}_i$ and $\vec{r}_i^p = \vec{r}_i - \vec{R}(t)$ are the position vectors of the electrons with respect to the target and the projectile, respectively. The relative projectile-target position vector $\vec{R}(t)$ defines the trajectories, with $\vec{R}(t) = \vec{b} + \vec{v}t$ in the usual straight-line, constant velocity approximation ($\vec{b}$ and $\vec{v}$ are respectively the impact parameter and the velocity; see Fig. 1). The potentials V_T and V_P describe the interactions between the electrons and, respectively, the target and projectile nuclei, i.e., $V_T(r_i) = -1/r_i$ and $V_P(r_i^p) = -2/r_i^p$ for the present system. The Schrödinger equation is solved by expanding the wave function onto a basis set composed of states of the isolated collision partners (i.e., asymptotic states), that is, in a general form,

$$\Psi(\vec{r}_1, \vec{r}_2, t) = \sum_{i=1}^{N_{TT}} c_i^{TT}(t) \Phi_i^{TT}(\vec{r}_1, \vec{r}_2) e^{-iE_i^{TT}t}$$

$$+ \sum_{j=1}^{N_{PP}} c_j^{PP}(t) \Phi_j^{PP}(\vec{r}_1, \vec{r}_2, t) e^{-iE_j^{PP}t}$$

$$+ \sum_{k=1}^{N_T} \sum_{l=1}^{N_P} c_{kl}^{TP}(t) \left[\phi_k^T(\vec{r}_1) \phi_l^P(\vec{r}_2, t) \right.$$

$$\left. \pm \phi_k^T(\vec{r}_2) \phi_l^P(\vec{r}_1, t) \right] e^{-i(E_k^T + E_l^P)t}, \tag{6}$$
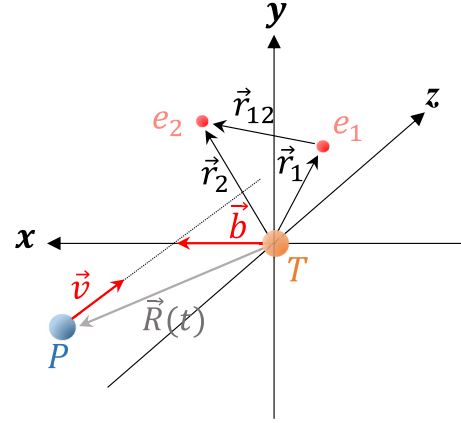
FIG. 1. Collision geometry. The impact parameter $\vec{b}$ and the velocity $\vec{v}$ define the collision plane (xz) and $\vec{R}(t)$ defines the projectile (P) trajectory with respect to the target (T). The positions of two electrons with respect to the target center are denoted $\vec{r}_1$ and $\vec{r}_2$, and $\vec{r}_{12} = \vec{r}_2 - \vec{r}_1$ is the relative vector between the two electrons. Note that in this figure we locate the origin of the reference frame on the target only for convenience since our equations are Galilean invariant.

where T and TT (P and PP) superscripts denote states and corresponding energies for which one and two electrons are on the target (projectile), respectively. Note that, in the present work, the two-electron states of target (H$^-$) are not included in the calculations, since the formation of H$^-$ in He$^+$-H collisions is expected to be negligible compared to the processes Eqs. (1)–(3). The $\pm$ sign in the last part of Eq. (6) stands for the singlet and triplet spin states, respectively, and the wave functions Φ_i^{TT} and Φ_j^{PP} are related to the corresponding spin symmetry. For both electrons, the projectile states contain plane-wave electron translation factors (ETFs), $e^{i\vec{v}\cdot\vec{r}_i - i\frac{1}{2}v^2 t}$, ensuring Galilean invariance of the results. The insertion of Eq. (6) into Eq. (4) results in a system of first-order coupled differential equations, which can be written in matrix form as

$$i\frac{d}{dt}\mathbf{c}(t) = \mathbf{S}^{-1}(\vec{b}, \vec{v}, t)\mathbf{M}(\vec{b}, \vec{v}, t)\mathbf{c}(t), \tag{7}$$

where $\mathbf{c}(t)$ is the column vector of the time-dependent expansion coefficients, i.e., c^{TT}, c^{PP}, and c^{TP} in Eq. (6); and $\mathbf{S}$ and $\mathbf{M}$ are the overlap and coupling matrices, respectively. We should emphasize here that we include explicitly in $\mathbf{M}$ all bielectronic couplings and, notably, the complex two-center ones which include the ETF for both electrons. We use the same strategy, i.e., no neglect of any couplings, to obtain the two-electron (PP) states in the diagonalization stage, going well beyond the Hartree-Fock approach. Our approach is, therefore, of the configuration interaction type, both statically and dynamically.

The coupled equations (7) are solved using the predictor-corrector variable-time-step Adams-Bashford-Moulton method for a set of initial conditions: initial state i, and given values of b and v. The probability of a transition $i \rightarrow f$ is given by the coefficients c_f ($\equiv c^{TT}$, c^{PP}, or c^{TP}) as

$$P_{fi}(b, v) = \lim_{t \to \infty} |c_f(t)|^2. \tag{8}$$

TABLE I. Parameters [angular momenta ℓ and exponents α, see Eq. (10)] of the GTOs included in two sets B1 and B2 to describe the electronic states of H, He$^+$ and He.

| | B1 | | | | B2 | | | |
| | H | | He$^+$ and He | | H | | He$^+$ and He | |
i	ℓ	α_i	ℓ	α_i	ℓ	α_i	ℓ	α_i
1	0	18.07493	0	184.20077	0	3.56102	0	27.05584
2	0	3.11302	0	27.05584	0	0.76810	0	5.80484
3	0	0.76102	0	5.80484	0	0.20833	0	1.62027
4	0	0.25810	0	1.62027	0	0.02020	0	0.58488
5	0	0.19833	0	0.58488	0	0.01578	0	0.15046
6	0	0.02920	0	0.15046	0	0.00657	0	0.02796
7	0	0.01578	0	0.10435	0	0.00183	1	3.02042
8	0	0.00657	0	0.02796	0	0.00029	1	0.85265
9	0	0.00183	0	0.02348	1	0.97651	1	0.29697
10	0	0.00029	0	0.00804	1	0.19740	1	0.12506
11	1	2.92000	1	12.69953	1	0.05330	1	0.04790
12	1	0.97651	1	3.02042	1	0.01514	1	0.02411
13	1	0.19740	1	0.85265	1	0.00838	2	0.13200
14	1	0.05330	1	0.29697	1	0.00258	2	0.04230
15	1	0.01513	1	0.12506	2	0.05259		
16	1	0.00838	1	0.04790	2	0.01458		
17	1	0.00258	1	0.02411	2	0.00375		
18	1	0.00105	1	0.01230	3	0.00657		
19	2	0.05259	2	0.18189				
20	2	0.01590	2	0.05486				
21	2	0.00556	2	0.01478				
22	2	0.00274						
23	3	0.00973						
24	3	0.00241						

The corresponding integral (total) cross sections for the considered transition are calculated as

$$\sigma_{fi}(v) = 2\pi \int_0^{+\infty} bP_{fi}(b, v)db. \qquad (9)$$

In our approach, in which total spin is conserved, the coupled equations (7) are solved independently for singlet and triplet symmetries corresponding to the two possible total spin states of the collision system. The spin-averaged cross sections are obtained as the sum of the singlet and triplet results according to their statistical weights, i.e., $\frac{1}{4}$ and $\frac{3}{4}$, respectively.

III. RESULTS AND DISCUSSION

To carry out the computations of cross sections for He$^+$-H collisions, we require to construct atomic states of H, He$^+$, and He to be included in the expansion equation (6). We express these states in terms of Gaussian-type orbitals (GTOs),

$$G_{\alpha,\ell,m}(\vec{r}) = r^\ell e^{-\alpha r^2} Y_{\ell,m}(\theta, \phi), \qquad (10)$$

for the one-electron [ϕ^T and ϕ^P in Eq. (6)] states and products of the same GTOs for the two-electron (Φ^{PP}) ones. The number of GTOs and their exponents α are optimized to get correct binding energies of the relevant states populated during the collision. In the present calculations, the GTO basis set B1 (see Table I) is used for both spin-singlet and spin-triplet symmetries. This basis set allows the inclusion of 1767 states and
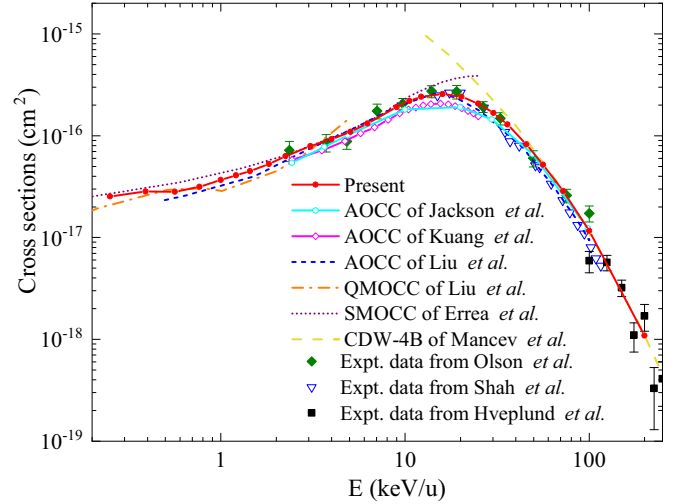
FIG. 2. Spin-averaged total electron capture cross sections as a function of impact energy. The theoretical results are as follows: the present calculations (red solid circles with a solid line), AOCC calculations of Jackson *et al.* [13] (cyan open hexagons with a solid line), Kuang *et al.* [17] (magenta open rhombuses with a solid line), Liu *et al.* [24] (blue dashed line), QMOCC calculations of Liu *et al.* [24] (orange dash-dotted line), SMOCC calculations of Errea *et al.* [8] (purple dotted line), and CDW-4B calculations of Mančev *et al.* [19] (yellow dashed line). The experimental results are from Olson *et al.* [3] (green solid rhombuses), Shah and Gilbody [33] (blue downward open triangles), and Hvelplund and Andersen [6] (black solid squares).

pseudostates [999 (H, He$^+$) and 768 (He) states] in the calculations for spin-singlet symmetry and the inclusion of 1729 states and pseudostates [999 (H, He$^+$) and 730 (He) states] for triplet symmetry. These states can describe elastic, single electron capture, excitation, and ionization through the inclusion of pseudostates with energy lying above ionization thresholds.

We have checked our results presented in the following by repeating the calculations with a smaller GTO set (B2, presented in Table I). For the electron capture processes reported in Sec. III A, the results from these two sets agree with each other within 1% for total capture and about 5% for selective capture to He($1s^2$) and He ($1s2\ell$ $^{1,3}L$) in the whole energy domain considered. For the cross sections of electron capture to He ($1s3\ell$ $^{1,3}L$), the convergence is about 20% at intermediate energies. For the lower- and higher-energy regions, the cross sections are rather small (down to 10^{-20} cm^2) and the differences reach up to 60%. For target excitation processes in both spin-singlet and spin-triplet cases reported in Secs. III B and III C, the convergence for excitation to H (2ℓ) is better than 5% in the whole considered energy region. The difference between the two series of cross sections for excitation to higher shells, H (3ℓ and 4ℓ), is about 7% at high energies when they reach their maximum, 26% at intermediate energies, and gets to 70% at the low energies, where, however, the cross sections are lower than 10^{-19} cm^2.

A. Total and He($1snℓ$)-selective electron capture cross sections

In Fig. 2, we present our calculated spin-averaged total electron capture cross sections as a function of impact
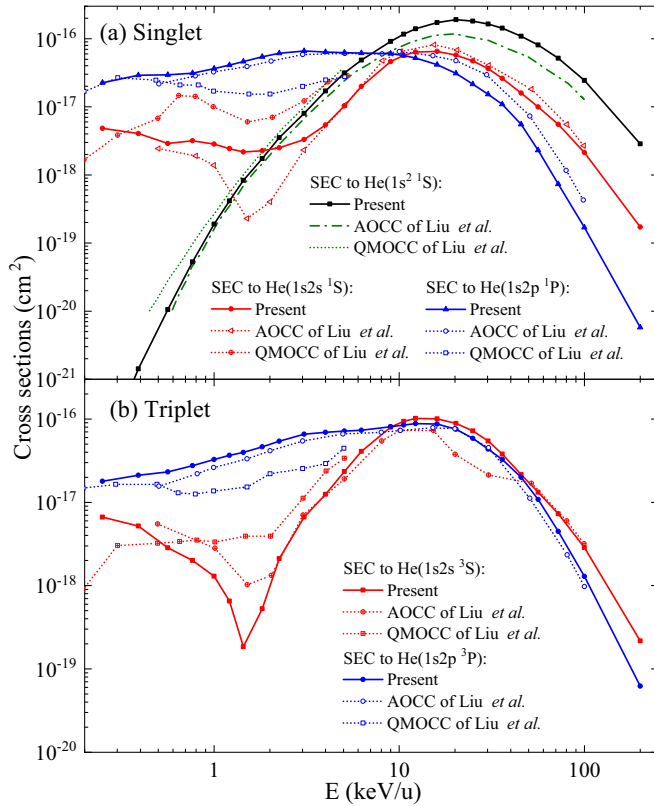
FIG. 3. Cross sections for electron capture to He($1s^2$ ^1S) and He($1s2\ell$ ^1L) in panel (a) and He($1s2\ell$ ^3L) in panel (b). Solid lines with solid symbols show the present results. Dotted and dashed lines with and without open symbols show the results from Liu *et al.* [24].

energy in the range 0.25–200 keV/u, together with previous experimental [3,6,33] and theoretical [8,13,17,19,24] results for comparison. As displayed in the figure, our cross sections agree very well with available experimental data [3,6,33]: a maximum is present at 15 keV/u, followed by a rapid decay for increasing energies. Compared with previous theoretical calculations, the AOCC cross sections reported in Refs. [13,17,24] follow the same trend as ours. However, the results of Jackson *et al.* [13] and Kuang *et al.* [17] lie slightly lower than ours and experimental data for energies around the maximum. This is probably due to insufficient channels included in the former calculations and to the single-electron approach used in the latter ones. In the low-energy range, our results agree reasonably well with those stemming from two methods known to be adequate in this range, i.e., the fully quantum molecular QMOCC approach [24] for $E < 3$ keV/u and the semiclassical molecular orbital one [8] for $E < 10$ keV/u. Finally, our results compare very well with those from CDW-4B calculations above 50 keV, below which this perturbative approach is not valid for the present collision system and, indeed, overestimates all available results.

We next investigate $n\ell$-selective electron capture to provide detailed information on the final-state distribution, which is of particular interest both in astrophysics and plasma diagnostics research since it determines the characteristics of the emitted radiation.

In Fig. 3, we present the cross sections for electron capture to the ground state He($1s^2$ ^1S), as well as to the He($1s2\ell$ $^{1,3}L$) levels. The available theoretical results from AOCC and QMOCC calculations of Liu *et al.* [24] are also displayed in the same figure for comparison. Our calculations show that electron capture to the excited He($1s2p$) states for the two spin symmetries dominate for low energies up to about 8 keV/u, while the production of He($1s^2$ ^1S) and He($1s2s$ ^3S) takes over at higher energies. We see important differences between our results and those from AOCC and QMOCC calculations [24]. For energies above 3 keV/u, the AOCC results seem to be in better agreement with ours, but, even here, we see significant deviations for electron capture to He($1s^2$ ^1S) and He($1s2s$ ^3S). Note that the AOCC is a single-active-electron approach, where the interaction between the active electron and the frozen open-shell He$^+(1s)$ is described by two different model potentials for the singlet and triplet symmetries. No interelectronic repulsion is therefore included in these calculations. On the other hand, the QMOCC calculations takes explicitly into account both electrons but only includes the lowest 12 $^{1,3}\Sigma$ and the 6 lowest $^{1,3}\Pi$ molecular states, covering asymptotically only up to H($n = 3$) and He($1s3\ell$) states. In our calculations, we consider explicitly the electronic static and dynamical correlations, using also a much more extended basis set. It is, therefore, not surprising to observe significant differences with these previous investigations, demonstrating further the importance of taking into account carefully the electronic repulsion as well as the couplings between higher excited states in order to reach reasonable convergence.

In Fig. 4, we present our cross sections for production of He($1s3\ell$) excited states for singlet and triplet symmetries, together with the only available calculations, i.e., the AOCC results of Liu *et al.* [24]. It can be observed that these cross sections are about 1 order of magnitude smaller than those of the He($1s2\ell$) production presented in Fig. 3. Though substantial discrepancies exist between our results and those reported in Ref. [24], these two series of data show quite similar energy dependencies and relative contributions of the different subshell 3ℓ production. Both predict that electron capture channels to He($1s3s$ ^1S and ^3S) dominate for energies above 10 keV/u. Below, the cross sections for the production of the various He($1s3\ell$) states get comparable until 1.5 keV/u, where the He($1s3s$) capture channels become the less likely ones. Note that the cross sections for the production of He($1s3\ell$ ^1L) show oscillations, in opposite phases for He($1s3p^1P$) and He($1s3d$ ^1D). The same is observed for triplet symmetry, but with a somewhat weaker amplitude. This latter behavior tends to indicate that the mechanisms leading to the different He($1s3\ell$) levels are coupled and interfere for both spin symmetries.

B. H(2ℓ)-selective target excitation

1. Cross sections

In Fig. 5, our spin-averaged cross sections for excitation to H($2s$) and H($2p$) are presented and compared with available theoretical [14,17,24] and experimental [4,15] results. Although slightly lower than experimental data for excitation to H($2p$), our cross sections show an overall good agreement with experiments for both channels. One can observe that the cross sections of excitation to H($2p$) show a rather weak
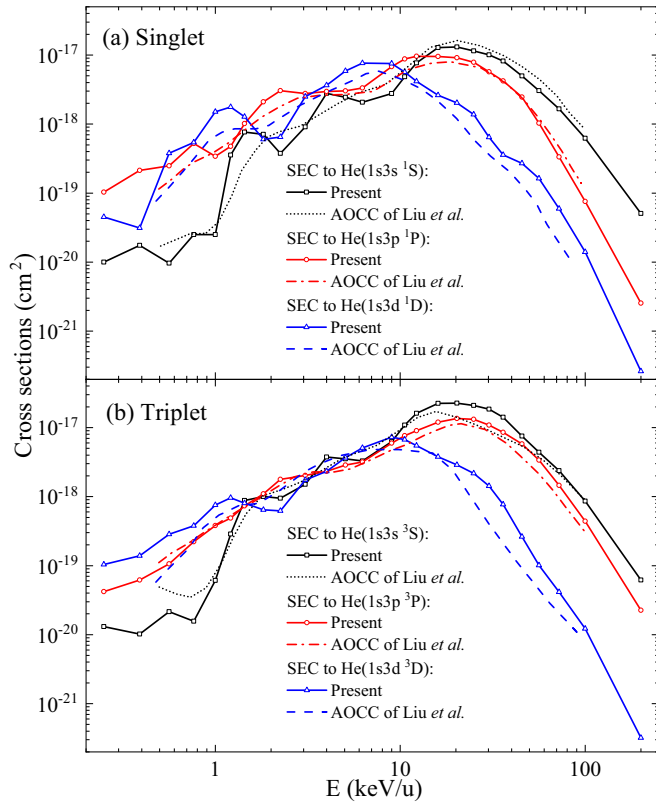
FIG. 4. Cross sections for electron capture to He($1s3\ell$ ^1L) in panel (a) and He($1s3\ell$ ^3L) in panel (b). Solid lines represent the present results. Dotted and dashed lines represent the AOCC results from Liu *et al.* [24].

energy dependence and magnitudes similar to the ones of the capture channels to excited He (see Figs. 3 and 4). In the whole energy range, H($2p$) production is the strongest target excitation channel, showing the dominant dipolar nature of the interaction with the projectile charge, as the nonrelativistic limit of the so-called Williams-Weizsäcker virtual photon method [39,40]. The present results agree reasonably well with the recent AOCC calculations of Ref. [24], especially for H($2p$) excitation. This fact tends to show that, compared to capture, the two-center electron-electron couplings (not included in Ref. [24]) exhibit here a rather small effect compared to the interaction with the projectile charge. On the other hand, compared to these two series of theoretical results and experimental data, the results from rather old AOCC approaches [14,17] show significant disagreements. The same conclusion can be drawn for the QMOCC calculations [24] for low energies. Finally it can be seen in Fig. 5 that the spin-averaged cross sections for both excitation to H($2s$) and H($2p$) show an oscillatory dependence structure as a function of impact energy. This behavior is more striking when inspecting the related cross sections for the two individual spin symmetries. This is shown in the next section, together with an interpretation.

2. Oscillatory dependence and Rosenthal model

To gain insight into the oscillatory structure, we present in Fig. 6 the magnetic sublevel populated cross sections for
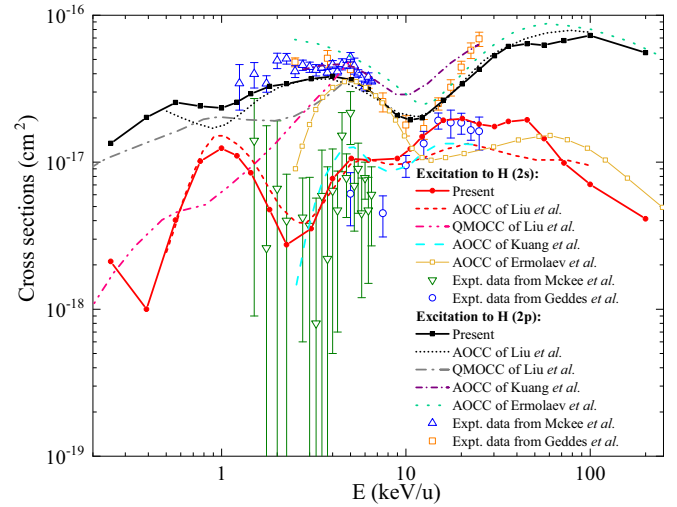
FIG. 5. Spin-averaged cross sections for target excitation to H($2s$) and H($2p$) as a function of impact energy. The present calculations are plotted as solid lines with symbols; the theoretical results from AOCC calculations of Liu *et al.* [24] for excitation to H($2s$) and H($2p$) are presented as red short-dashed and black short-dotted lines, respectively; the QMOCC calculations of Liu *et al.* [24] for excitation to H($2s$) and H($2p$) are plotted as magenta dash-dot-dotted and gray long-dash-dotted lines, respectively; the AOCC calculations of Kuang *et al.* [17] are plotted as cyan long-dashed and purple short-dash-dotted lines; the AOCC calculations of Ermolaev *et al.* [14] are plotted as a green dotted line and a yellow line with open squares. The experimental results of McKee *et al.* [4] and Geddes *et al.* [15] are shown as symbols and error bars.

excitation to H($2\ell_0$) (for total spin-singlet symmetry) and electron capture to He($1s2p$ ^1P, $|M_L| = 1$) as a function of the inverse of the velocity ($1/v$). It can be observed that the cross sections for excitation to H($2s$) and H($2p_0$) show clear oscillations in the opposite phase, like the cross sections of capture to He($1s2p$ ^1P, $|M_L| = 1$) with the H($2p_1$) excitation
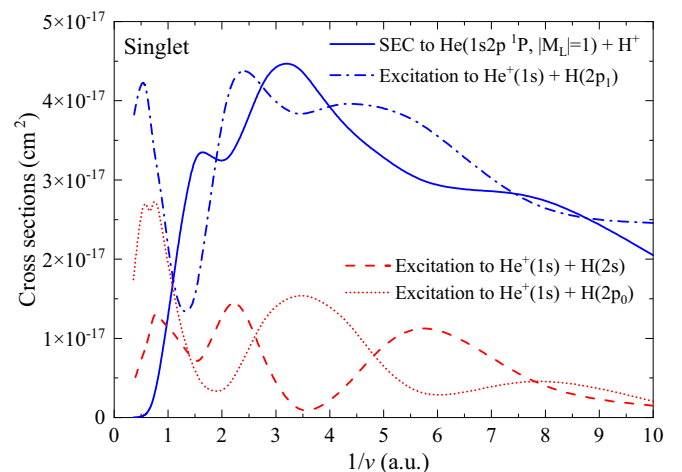
FIG. 6. Magnetic sublevel populated cross sections as a function of the inverse of the velocity ($1/v$) for excitation to H($2s$, $2p_0$, and $2p_1$) in the spin-singlet symmetry and electron capture to He($1s2p$ ^1P, $|M_L| = 1$).
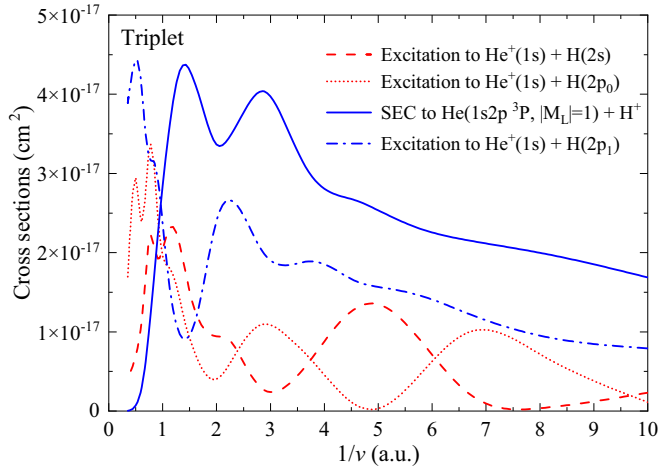
FIG. 7. Magnetic sublevel populated cross sections as a function of the inverse of the velocity ($1/v$) for excitation to H($2s$ and $2p_0$) in the spin-triplet symmetry and electron capture to He($1s2p$ ^3P, $|M_L| = 1$).

ones. This suggests that the oscillatory patterns stem from coherence effects between the considered channels. In fact, such oscillatory structure in the cross sections can be explained by Rosenthal and Foley's model [41] and have been observed previously (i) for excitation of helium by helium-ion impact [41] (see also Ref. [42]), (ii) for ionization and negative-ion formation in H + H collisions [43], (iii) for excitation cross sections in ion-hydrogen collisions [44] (using a somewhat different model but based on a molecular representation of the collision system and interferences between different paths within the molecular energy curves), and (iv) recently, for double-electron capture in H$^+$ + H$^-$ [45] and H$^+$ + Mg [46] collisions. In the model proposed in Refs. [41,42] the

oscillations are interpreted through a molecular representation of the scattering event. It involves three molecular energy curves of the collision system and two avoided crossings in an adiabatic picture (see Fig. 7 in Ref. [42]). The curve correlated asymptotically to the initial channel crosses at small internuclear distances (R_x) the curves correlated to the two inelastic channels considered. Through these transitions, the system evolves along two different molecular states until these latter ones couple again at a crossing occurring at large distances ($R_0 > R_x$). In this model, the amplitude of each pathway acquires a different phase in the internuclear distance region where the curves cross, i.e., between R_x and R_0. At the latter distance, the amplitudes of the two inelastic channels are then coherently mixed, which may lead to an interference pattern and then to the oscillations of the cross sections. The period of the oscillations is given by the cumulated energy difference ΔE between the two molecular states between R_x and R_0,

$$T = \frac{2\pi}{\int_{R_x}^{R_0} \Delta E \, dR},\tag{11}$$

when presented as functions of $1/v$.

We have generated potential energy curves of the HeH$^+$ molecular ion using full configuration interaction calculations with the same basis set as in the SCASCC calculations. In Fig. 8(a) (singlet total spin), we present a selection of the important states converging asymptotically to the initial channel ($2\,^1\Sigma$), excitation He$^+$($1s$) + H($n = 2$) ($3, 4, 5\,^1\Sigma$, $1\,^1\Pi$), and capture He($1s2p$ ^1P, $|M_L| = 1$) + H$^+$ ($2\,^1\Pi$). The energy difference between the states ($5\,^1\Sigma$-$4\,^1\Sigma$ and $2\,^1\Pi$ -$1\,^1\Pi$) considered in the following are shown as hatches, in red and blue, respectively.

In the course of the collision, as the target and projectile approach each other, the system evolves on the $2\,^1\Sigma$ curves, and transitions to $4\,^1\Sigma$ and $5\,^1\Sigma$ (also to $1\,^1\Pi$ and $2\,^1\Pi$) will
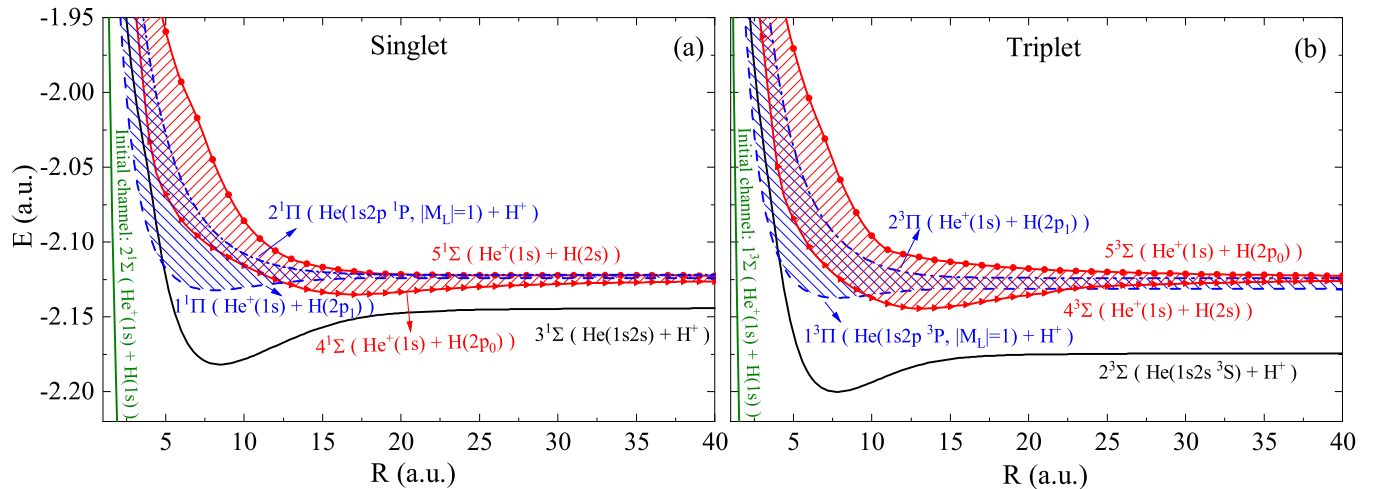
FIG. 8. Adiabatic potential energy curves of the HeH$^+$ molecular ion for singlet (a) and triplet (b) spin symmetries. (a) The molecular energy curves correlated asymptotically to He$^+$($1s$) + H($2s$ and $2p_0$) ($4\,^1\Sigma$ and $5\,^1\Sigma$) are shown with red symbols, the pathways correlated asymptotically to excitation to H($2p_1$) and electron capture to He($1s2p$ ^1P, $|M_L| = 1$) ($1\,^1\Pi$ and $2\,^1\Pi$) are shown as blue dashed and dash-dotted lines, respectively. Their energy differences are highlighted by read and blue hatches, respectively. The molecular curves related to the initial channel ($2\,^1\Sigma$) and capture to He($1s2s$) ($3\,^1\Sigma$) are also shown, in green and black, respectively. (b) The molecular energy curves correlated to the same asymptotic channels (for their triplet counterparts) are shown with the same color and symbols. Same as in panel (a) for the hatched area.

take place at the inner repulsive wall ($R_x \approx 1$ a.u.). On the way out, each pathway acquires a different phase according to the energy of the populated molecular state and is coherently mixed at a large internuclear distance, $R_0 \approx 40$ a.u, the results being independent of the exact values of the two crossing locations since the cumulated energy difference is mainly stemming from the region from 2 to 25 a.u. Using Eq. (11) and the energy differences shown with hatched areas in Fig. 8(a), the period of the oscillations is about 6.0 a.u. for excitation to H($2s$) and H($2p_0$) ($5\,^1\Sigma$-$4\,^1\Sigma$) and is about 6.3 a.u. for electron capture to He($1s2p\,^1P$, $|M_L| = 1$) and excitation to H($2p_1$) ($2\,^1\Pi$-$1\,^1\Pi$). These periods agree well with the *ab initio* calculations shown in Fig. 6, which predict a period of about 5–6 a.u. for both excitation to H($2s$) and H($2p_0$), as well as electron capture to He($1s2p\,^1P$, $|M_L| = 1$) and excitation to H($2p_1$) at large $1/v$ ($1/v > 2$), i.e., at low velocities for which a molecular representation is appropriate. This supports the Rosenthal mechanism to explain the observed oscillatory structures in the cross sections.

In Fig. 7, we present the cross sections for excitation to H($2s$) and H($2p_0$) as function of the inverse of the velocity in the case of triplet total spin symmetry. It can be seen that these cross sections show an oscillatory behavior in opposite phases, with a period of about 4–5 a.u. for large $1/v > 2$. As for singlet total spin, Fig. 8(b) presents the potential energy curves for the triplet case: among others are shown the important $4\,^3\Sigma$ and $5\,^3\Sigma$ states, correlated asymptotically to H($2s$) and H($2p_0$) excitation, as well as the $1\,^3\Pi$ and $2\,^3\Pi$ states, correlated asymptotically to electron capture to He($1s2p\,^3P$, $|M_L| = 1$) and to H($2p_1$) excitation. Following the Rosenthal model and the energy difference between the $4\,^3\Sigma$ and $5\,^3\Sigma$ states [red hatching in Fig. 8(b)], the calculated period is found to be about 5.0 a.u, showing again a good agreement with the close-coupling results. Moreover one can observe that, contrary to the singlet case, the two Π curves (in blue) are parallel asymptotically and therefore do not cross at large internuclear distance so that Rosenthal's double-crossing model is not fulfilled: the cross sections for the two channels of capture to He($1s2p\,^3P$, $|M_L| = 1$) and to H($2p_1$) excitation do not show indeed oscillatory behavior for large $1/v > 4$.

We may conclude that the oscillations observed in the cross sections for excitation to H($2s$) and H($2p$) shown in Fig. 5 for impact energy smaller than, say, 10 keV/u stem from interferences between excitation to H($2s$) and H($2p_0$) in both spin-singlet and spin-triplet symmetries. This mechanism of molecular nature leading to interferences and oscillations in cross sections is also demonstrated between capture and excitation processes, leading to the production of, respectively, He($1s2p\,^1P$, $|M_L| = 1$) and H($2p_1$) in the spin-singlet symmetry.

Finally, note that oscillatory structures in excitation cross sections and capture ones for one-electron and quasi-one-electron systems have been previously attributed to swaps of the electron between the target and projectile nuclei during the collisions in a classical picture (see, for example, Refs. [47,48]). However in these investigations illustrated by classical trajectory Monte Carlo calculations, oscillations in opposite phases for two specific channels were not discussed and even observed and therefore cannot be advocated for the present case.
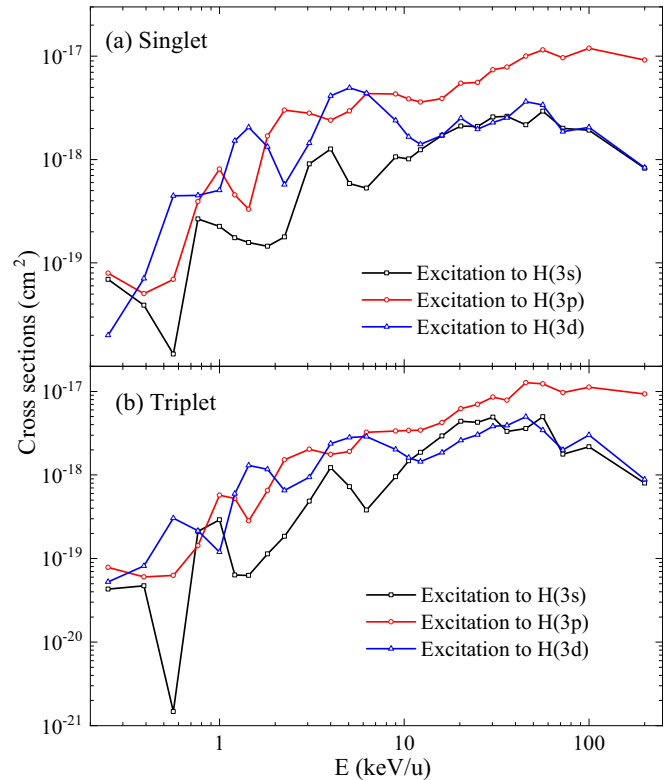
FIG. 9. Cross sections for target excitation to H(3ℓ) as a function of impact energy in spin-singlet (a) and spin-triplet (b) symmetries.

C. H(3ℓ)- and H(4ℓ)-selective target excitation cross sections

We have further investigated the target excitation to higher states. In Figs. 9 and 10, we show our cross sections for excitation to, respectively, H(3ℓ) and H(4ℓ) as a function of the impact energy. For energies higher than 10 keV/u, excitations to H($3p$) and H($4p$) are the dominant channels as expected, but in a weaker proportion than the one observed for H($n = 2$) excitation in Fig. 5. For decreasing energies, the cross sections for the different angular momenta become comparable within each given shell. It is interesting to note that Rosenthal-like out-of-phase oscillations can also be observed between these excitation channels but a simple analysis with Eq. (11) cannot be drawn for these manifolds. The only available experimental data relevant to H(3ℓ) excitation in He$^+$-H collisions are indirect and correspond to the measurements of the Balmer H$_\alpha$ emission cross sections by Donnelly *et al.* [11]. Using the corresponding branching ratio, these results can be expressed in terms of our 3ℓ-selective excitation cross sections [$\sigma(3\ell)$] as $\sigma(\text{H}_\alpha) = \sigma(3s) + 0.12\sigma(3p) + \sigma(3d)$, neglecting the possible cascade for higher shells which should be weakly populated as can be already seen for the 4ℓ shell in Fig. 10.

We present our H$_\alpha$ emission cross sections evaluated by using the above formula, together with previous calculations [13,17,24] and the experimental data of Donnelly *et al.* [11] in Fig. 11. Large discrepancies can be observed between the available calculations though they stem from equivalent atomic-orbital approaches. It should be mentioned that the calculations in Refs. [17,24] are based on a single-active-electron approach while the results reported in Ref. [13] are obtained
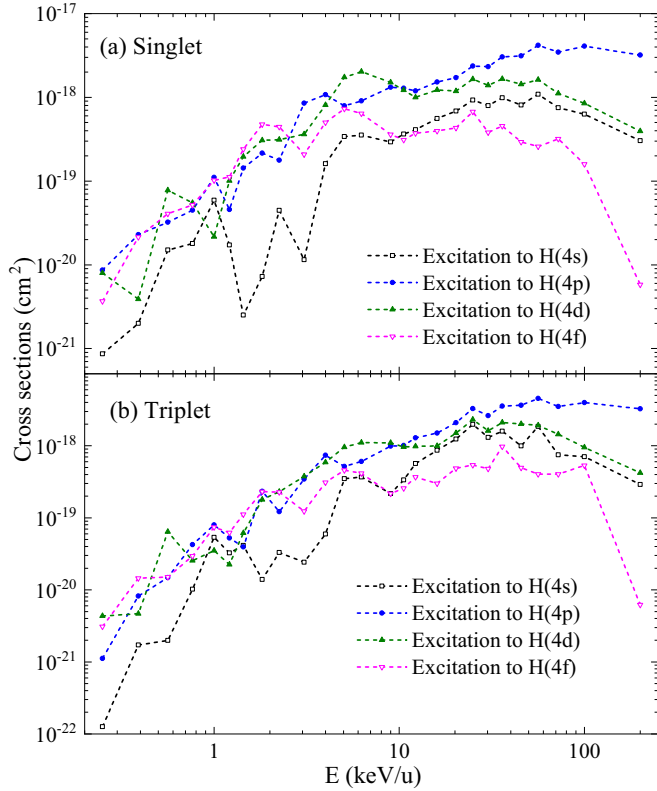
FIG. 10. Cross sections for target excitation to H(4ℓ) as a function of impact energy in spin-singlet (a) and spin-triplet (b) symmetries.

from a two-active-electron approach but with a limited basis (39 singlet states and 38 triplet ones) in the calculations. We emphasize that our two-active-electron calculations are the most elaborate ones in terms of accounting for electronic correlations and open channels. However, it can be observed
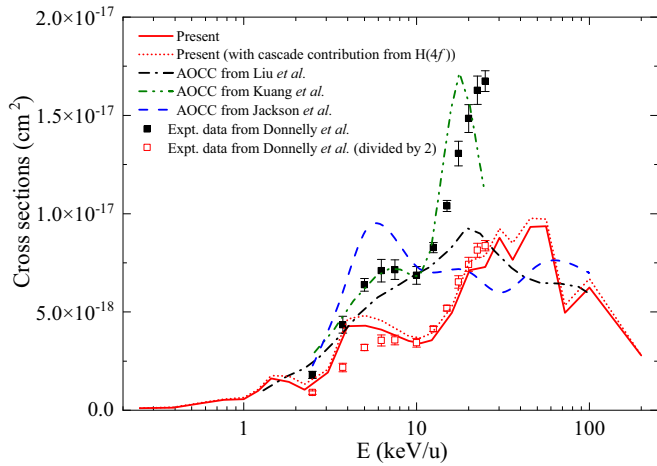
FIG. 11. Balmer H$_\alpha$ emission cross sections in He$^+$ and H collisions as a function of the impact energy. The present results with or without the cascade contribution from H($4f$) are compared with experimental data of Donnelly *et al.* [11] divided by 2 or not and theoretical calculations of Liu *et al.* [24], Kuang *et al.* [17], and Jackson *et al.* [13].

from Fig. 11 that our results underestimate the experimental data [11], especially for energies higher than 5 keV/u, by about a factor of 2. As mentioned in Ref. [11], the cross sections were not corrected for the cascade contributions from higher levels, mainly from H($4f$) (the radiative decay fractions for other states are negligible according to Ref. [49]), which would enhance H$_\alpha$ emission cross sections. The present summed cross sections of H$_\alpha$ emission and H($4f$) excitation are also shown in Fig. 11 (red dotted line). However, this correction does not change significantly the results since the contribution from H($4f$) is evaluated to be smaller than 12% in our calculations, supporting the estimation of 15% reported in Refs. [11,49]. However, the experimental data of Donnelly *et al.* [11] were determined by normalization with previous measurements [49] for H$^+$ and H$_2$ collisions at 40 keV, which themselves were normalized to the absolute measurement of Lenormand [50] for electron capture to H($3s$) in H$^+$ + Ar collisions at 20 keV. The cross section in the measurement of Lenormand [50] is reported to be about 9.8×10^{-18} cm^2, which overestimates by a factor of about 2 the experimental results from two independent studies, Hughes *et al.* [51] and Renwick *et al.* [52], in which this cross section was measured to be 5.2×10^{-18} cm^2, within an $\approx$30% uncertainty (in Ref. [52]). This suggests that the experimental data of Donnelly *et al.* [11] overestimate the Balmer H$_\alpha$ emission cross sections by this factor 2 due to the normalization procedure. In Fig. 11 we show as red open squares the experimental data divided by this factor. With this correction a good agreement with our results is seen, both in magnitude and shape, especially above 10 keV/u. This convergence and the fact that the other theoretical results, except for Ref. [17], predicted cross sections lower than 10^{-17} cm^2 legitimate the renormalization of the results of Donnelly *et al.* [11].

IV. CONCLUSIONS

Using a two-active-electron close-coupling approach with a configuration interaction treatment to deal with electronic correlation, we have investigated electron capture and target excitation processes in He$^+$-H collisions. In the energy region 0.25–200 keV/u, total and state-selective cross sections in both spin-averaged and spin-resolved cases have been reported and compared with available theoretical and experimental data. Our results show the best agreement with the experimental ones in the different energy ranges available. This demonstrates the importance of a two-electron treatment taking into account electronic correlation and the use of an extended basis set spanning more than the states considered, within a close-coupling scheme. Furthermore, our investigation suggests that the oscillatory structures observed in the cross sections for excitation to H($2s$) and H($2p$) come from interferences between excitation to H($2s$) and H($2p_0$) in both spin-singlet and spin-triplet symmetries, as well as interferences between the electron capture He($1s2p$ ^1P, $|M_L| = 1$) channel and H($2p_1$) excitation in the spin-singlet symmetry.

We have also extended the understanding of this collision system for electron capture and excitation channels to excited states up to $n = 4$. However, the only available measurements of nonabsolute cross sections of Balmer H$_\alpha$ emission [11] turned out to be about 2 times larger than our results. This

discrepancy has been attributed to the normalization procedure used in this investigation. Using a normalization based on cross sections reported in two independent experimental works, our results show a good agreement. Further experimental or theoretical investigations would be useful to draw definite conclusions.

[1] R. A. Young, R. F. Stebbings, and J. W. McGowan, Phys. Rev. **171**, 85 (1968).

[2] J. Fayeton, J. C. Houver, M. Barat, and F. Masnou-Seeuws, J. Phys. B **9**, 461 (1976).

[3] R. E. Olson, A. Salop, R. A. Phaneuf, and F. W. Meyer, Phys. Rev. A **16**, 1867 (1977).

[4] J. D. A. McKee, J. R. Sheridan, J. Geddes, and H. B. Gilbody, J. Phys. B **10**, 1679 (1977).

[5] J. E. Aldag, J. L. Peacher, P. J. Martin, V. Sutcliffe, J. George, E. Redd, T. J. Kvale, D. M. Blankenship, and J. T. Park, Phys. Rev. A **23**, 1062 (1981).

[6] P. Hvelplund and A. Andersen, Phys. Scr. **26**, 375 (1982).

[7] D. Bordenave-Montesquieu, P. Nouet, A. Boutonnet, C. Bergnes, and R. Dagnac, J. Phys. B **20**, 4493 (1987).

[8] L. Errea, L. Méndez, and A. Riera, Z. Phys. D **14**, 229 (1989).

[9] R. Hippler, H. Madeheim, H. O. Lutz, M. Kimura, and N. F. Lane, Phys. Rev. A **40**, 3446 (1989).

[10] A. Bordenave-Montesquieu, M. Boudjema, P. Benoit-Cattin, A. Gleizes, and P. Moretto-Capelle, J. Phys., Colloq. **50**, C1-305 (1989).

[11] A. Donnelly, J. Geddes, and H. B. Gilbody, J. Phys. B: At. Mol. Opt. Phys. **24**, 165 (1991).

[12] L. F. Errea, A. Lopez, L. Mendez, and A. Riera, J. Phys. B: At. Mol. Opt. Phys. **25**, 811 (1992).

[13] D. Jackson, H. A. Slim, B. H. Bransden, and D. R. Flower, J. Phys. B: At. Mol. Opt. Phys. **25**, L127 (1992).

[14] A. M. Ermolaev, D. Jackson, N. Shimakura, and T. Watanabe, J. Phys. B: At. Mol. Opt. Phys. **27**, 4991 (1994).

[15] J. Geddes, A. Donnelly, M. P. Hughes, D. P. Higgins, and H. B. Gilbody, J. Phys. B: At. Mol. Opt. Phys. **27**, 3037 (1994).

[16] L. F. Errea, L. Mendez, and A. Riera, J. Phys. B: At. Mol. Opt. Phys. **28**, 907 (1995).

[17] J. Kuang, Z. Chen, and C. D. Lin, J. Phys. B: At. Mol. Opt. Phys. **28**, 2173 (1995).

[18] J. B. Wang, J. P. Hansen, and A. Dubois, Phys. Rev. Lett. **85**, 1638 (2000).

[19] I. Mančev, Phys. Rev. A **75**, 052716 (2007).

[20] V. Shevelko, D. Kato, M.-Y. Song, H. Tawara, I. Tolstikhina, and J.-S. Yoon, Nucl. Instrum. Methods Phys. Res. Sect. B **267**, 3395 (2009).

[21] S. Azizan, F. Shojaei, and R. Fathi, J. Phys. B: At. Mol. Opt. Phys. **49**, 085201 (2016).

[22] S. Azizan, F. Shojaei, and R. Fathi, J. Phys. B: At. Mol. Opt. Phys. **49**, 135201 (2016).

[23] N. Milojević, I. Mančev, and D. Belkić, Phys. Rev. A **96**, 032709 (2017).

[24] L. Liu, X. Lin, Y. Wu, J.-G. Wang, and R. K. Janev, Eur. Phys. J. D **71**, 1 (2017).

[25] J. Loreau, S. Ryabchenko, J. M. M. Burgos, and N. Vaeck, J. Phys. B: At. Mol. Opt. Phys. **51**, 085205 (2018).

[26] Y. J. Rivera, E. Landi, S. T. Lepri, and J. A. Gilbert, Astrophys. J. **899**, 11 (2020).

[27] P. Swaczyna, D. McComas, and E. Zirnstein, Astrophys. J. **875**, 36 (2019).

[28] F. B. Rosmej, R. Stamm, and V. S. Lisitsa, Europhys. Lett. **73**, 342 (2006).

[29] A. A. Korotkov and R. K. Janev, Phys. Plasmas **3**, 1512 (1996).

[30] H. Anderson, M. Von Hellermann, R. Hoekstra, L. Horton, A. Howman, R. Konig, R. Martin, R. Olson, and H. Summers, Plasma Phys. Controlled Fusion **42**, 781 (2000).

[31] E. Delabie, M. Brix, C. Giroud, R. Jaspers, O. Marchuk, M. O'Mullane, Y. Ralchenko, E. Surrey, M. Von Hellermann, K. Zastrow, and JET-EFDA Contributors, Plasma Phys. Controlled Fusion **52**, 125008 (2010).

[32] Atomic and Plasma-Material Interaction Data for Fusion, edited by R. E. H. Clark (IAEA, Vienna, 2001).

[33] M. B. Shah and H. B. Gilbody, quoted as private communication in Ref. [19].

[34] G. W. McClure, Phys. Rev. **148**, 47 (1966).

[35] N. Sisourat, I. Pilskog, and A. Dubois, Phys. Rev. A **84**, 052722 (2011).

[36] J. W. Gao, Y. Wu, N. Sisourat, J. G. Wang, and A. Dubois, Phys. Rev. A **96**, 052703 (2017).

[37] Y. W. Zhang, J. W. Gao, Y. Wu, J. G. Wang, N. Sisourat, and A. Dubois, Phys. Rev. A **106**, 042809 (2022).

[38] J. W. Gao, Y. Y. Qi, Y. Wu, and J. G. Wang, Astrophys. J. **944**, 167 (2023).

[39] C. F. V. Weizsäcker, Z. Phys. **88**, 612 (1934).

[40] E. J. Williams, Mat.-Fys. Medd.–K. Dan. Vidensk. Selsk. **13**, 4 (1935).

[41] H. Rosenthal and H. M. Foley, Phys. Rev. Lett. **23**, 1480 (1969).

[42] H. Rosenthal, Phys. Rev. A **4**, 1030 (1971).

[43] S. Y. Ovchinnikov, Y. Kamyshkov, T. Zaman, and D. R. Schultz, J. Phys. B: At. Mol. Opt. Phys. **50**, 085204 (2017).

[44] P. S. Krstic, C. O. Reinhold, and D. R. Schultz, J. Phys. B: At. Mol. Opt. Phys. **31**, L155 (1998).

[45] J. W. Gao, Y. Wu, J. G. Wang, A. Dubois, and N. Sisourat, Phys. Rev. Lett. **122**, 093402 (2019).

[46] J. W. Gao, Y. Y. Qi, Z. H. Yang, Z. M. Hu, Y. W. Zhang, Y. Wu, J. G. Wang, A. Dubois, and N. Sisourat, Phys. Rev. A **104**, 032826 (2021).

[47] D. R. Schultz, C. O. Reinhold, and P. S. Krstić, Phys. Rev. Lett. **78**, 2720 (1997).

[48] S. Otranto, R. Hoekstra, and R. E. Olson, Phys. Rev. A **89**, 022705 (2014).

[49] I. D. Williams, J. Geddes, and H. B. Gilbody, J. Phys. B **15**, 1377 (1982).

[50] J. Lenormand, J. Phys. Fr. **37**, 699 (1976).

[51] R. H. Hughes, C. A. Stigers, B. M. Doughty, and E. D. Stokes, Phys. Rev. A **1**, 1424 (1970).

[52] S. P. Renwick, E. C. Martell, W. D. Weaver, and J. S. Risley, Phys. Rev. A **48**, 2910 (1993).